Design and Integration of a Flapping Wing Apparatus

Bradley Rayman, Badih Jawad, Hamid Vejdani*

Bio-Inspired Robotics and Dynamics (BIRD) lab Mechanical, Robotics, and Industrial Engineering Department Lawrence Technological University Southfield, Michigan Email: hvejdanin@ltu.edu

In this paper we presented the design, integration and experimental verification of a flapping wing apparatus. The purpose for this apparatus is to provide a framework to study the applicability of various types of sensors on flapping wings in the presence of forward speed. This work is inspired by the discoveries of mechanosensory hairs on insect wings that perform like strain-gauge sensors. To design the apparatus, we started by kinematic analysis of a crank-slider mechanism to actuate the wings. After that, we constructed the equations of motion of the entire system to find the proper gear ratio, motor properties and other geometric dimensions. For the aerodynamic modeling, we used a quasi-steady formulation and presented a closed form solution for the aerodynamic torque. Then, we explained the integration process and manufacturing of the main parts and presented two prototypes for the apparatus. At the end, we showed the final constructed versions of the apparatus and presented the experimental response and compared them with the simulation.

1 Introduction

The outstanding performance of natural fliers have inspired the development of flapping wing aerial vehicles (FWAVs) [1–5]. In nature, bats, insects, and birds excel at different modes of flight in a robust and efficient way compared to developed flapping flying robots [1, 3, 4, 6]. One of the challenges is the complexity of the biological structures which makes it difficult to mimic and replicate in an engineering system. For example, the variety, distribution and applicability of various sensors available on natural fliers' wing although seems to be critical but are not thoroughly understood. Bat and insect wings include many sensors like strain sensors, air flow sensors and speed sensors [7–9] which provide crucial information during the flight (Fig. 1). We seek to understand the applicability of wing sensors and in particular strain sensors during flapping flight and specially on wings with variable flexibility. Therefore, the goal in this paper is to present the design, manufacturing and inte-

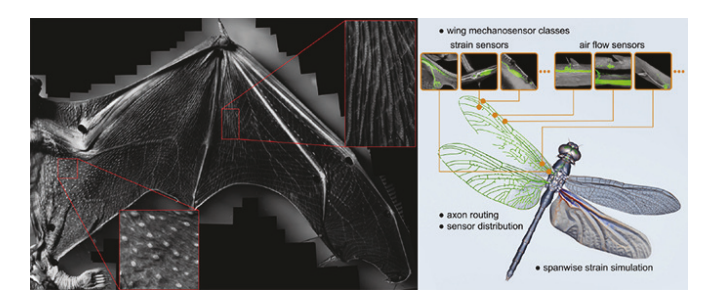


Fig. 1. Natural fliers carry various sensors on their wings. Left: bat wing [8], right: dragonfly wing [9]

gration of a flapping wing apparatus to be used as a test bed for this purpose.

The majority of the flapping wing robots use either external real-time tracking sensors or internal sensors on the body like inertia measurement unit (IMU), rotary encoders, and GPS. Some of the notable accomplishments include COLIBRI [10], KUBeetle [6], Robobee [11], Delfly II [12], BatBot [1], and hummingbird robot [2]. Wood et al. [3] developed an insect scale flapping wing robot that later Chirarattananon et al. [13] showed is capable of hovering in the presence of wind gusts. They used piezoelectric actuators directly connected to the wings and used real-time tracking of the different points on the robot as the main sensory information. Tu et al. [2] presented the design and prototyping of a hummingbird scale robot with two electric motors that each directly controls one wing. In their robot, the motor is connected to the wing through two gear spurs and therefore to generate flapping motion, motors should rotate and brake regularly. For the sensory information, they used IMU to measure the orientation of the body. He et al. [4] introduced a bird-scale flapping wing robot with 3 actuators total. They used spatial four bar mechanism to actuate the two wings with one motor and presented the kinematics and dynamics of their design. Ramezani et al. [1] designed a tailless batscale flapping wing robot and demonstrated remarkable capabilities including banking and turning maneuvers. In these examples, the common approach is to focus on measuring the orientation of the body as the main source of sensory information.

In natural fliers, there are redundant availability of sensory signals [8, 9]. Figure 1 shows two examples of bat and dragonfly wings with variety of sensors spread along them. However, it is not practical to provide that many sensors on a robotic system due to the increase in computational and building cost. Therefore, recognizing the important sensory signals in natural fliers and exploiting the use of the information to its utmost potential during flight is critical.

In this work we aim at designing an apparatus as a framework on which to install various types of sensors on the wings and study their potential in providing flight information. This framework is aimed to be installed in a wind tunnel shown in Fig. 2. Moreover, we intend to use those sensors during flapping to study the effect of wing material texture and flexibility on aerodynamic force distribution. To design the apparatus, we first select the proper mechanism by comparing different alternatives for flapping wing systems and select the one that is the most suitable for our purpose. Then, we use the kinematic analysis to properly design the geometry of the mechanism accompanied by the dynamics of the entire system to model the behavior of the mechanism more accurately. We construct the dynamics of the entire apparatus using Lagrangian formulation and include the dynamics of the motor (both mechanical and electrical equations). After that, we present the aerodynamic modeling for the design purpose. Then we present the process for trade-off between the gear ratio, and motor characteristics. Then we present the manufacturing process for the different parts of the apparatus and explain the decision makings.

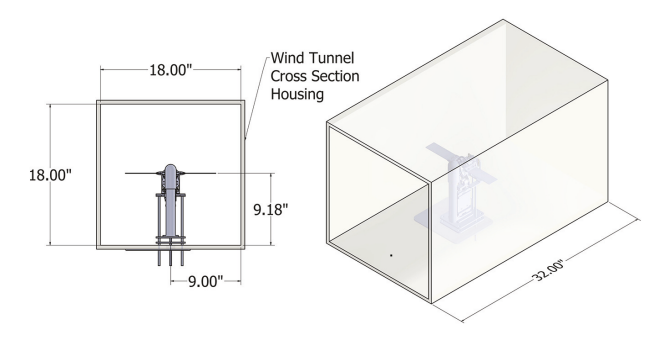


Fig. 2. The overall setup of the experiments and the wind tunnel dimensions for the apparatus size constraints.

2 Mechanism Design

Our goal for this apparatus is to generate flapping motion on the two wings identically with minimal vibrations from the moving parts. To achieve identical flapping motion on the wings, we targeted mechanisms that are able to generate the same motion on the two wings using the proper mechanical mechanism of the system actuated by a single

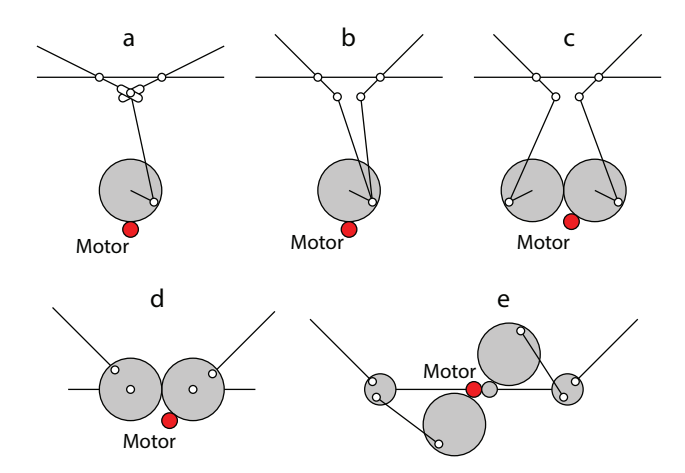


Fig. 3. The different types of the motor to wing connection mechanisms. a) crank-slider mechanism, b) single-crank double-rocker mechanism, c) double-crank double-rocker mechanism, d) gearbox (transmission) direct connection, and e) four-bar linkage mechanism. The motor is shown as a red circle and the gray circles are the gears.

motor. Therefore, given the size constraints and goals of the apparatus, we consider the mechanisms shown in Fig. 3. In this figure the mechanisms are: a) crank-slider mechanism, b) single-crank double-rocker mechanism, c) double-crank double-rocker mechanism, d) gearbox (transmission) direct connection, and e) four-bar linkage mechanism. The crankslider mechanism (Fig. 3-a) can provide narrow width for the apparatus to minimize the interference to the flow in the wind tunnel while creating the identical flapping motion on the two wings. We can change the flapping angle amplitude in this mechanism, and a symmetrical down-stroke and upstroke motions can be easily generated by the mechanism. The single-crank double-rocker mechanism (Fig. 3-a) is similar to the crank-slider mechanism from the apparatus width point of view, however it generates a phase difference between the motion of the two wings. Moreover, the sliders are free and oscillates in horizontal direction during a wingbeat which applies undesired lateral vibration to the entire apparatus. The double-crank double-rocker mechanism shown in Fig. 3-c resolves the problem with nonidentical wing motions but requires wider width for the apparatus and also imposes more moving parts to the mechanism making this less desirable compared to the crank-slider mechanism. From the kinematics point of view, it is similar to the four-bar linkage mechanism which we discuss later. The third mechanism that we consider is the direct gearbox (connection) between the motor and the wings as shown in Fig. 3-d. In this mechanism the motor directly controls the wings through the gearbox which requires the motor to repeatedly reverse direction in order to generate flapping motion on the wings. This back and forth spinning motion of the motor applies undesired vibrations on the apparatus due to the inertia of the motor and the reflected inertia of the gearbox [2, 14]. Moreover, the required width of the mechanism is increased. The last mechanism that we consider is a four-bar linkage shown in Fig. 3-e. This mechanism allows for the two wings to move identical as the motor spin continuously in one direction. However,

Wing motion in a wingbeat cycle

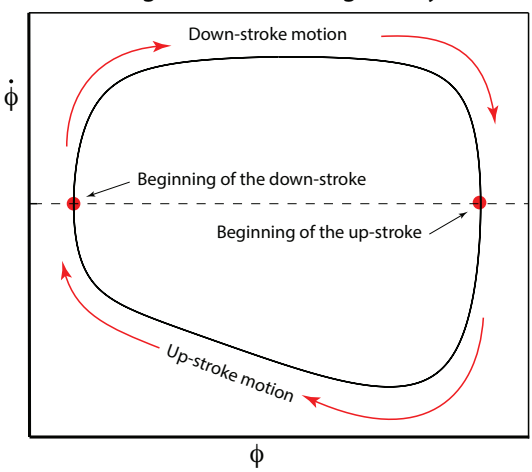


Fig. 4. The kinematics of the wing during a wingbeat cycle generated by the four-bar linkage mechanism under a constant motor velocity. The upstroke and down-stroke motions are not symmetrical.

beside the increased in the width of the apparatus, this mechanism has a singularity at the beginning and end of the upstroke and down-stroke. This singularity imposes an asymmetrical motion with respect to each stroke as shown in Fig. 4 [15]. This figure shows how the flapping angle and its velocity change during a wingbeat cycle. As can be seen, the upstroke and the down-stroke are not symmetrical. Moreover, the four-bar linkage mechanism is more sensitive to the resolution manufacturing of the parts [15]. This is due to the singular point in the mechanism that makes the flapping motion possible with unidirectional spinning of the motor. The flapping angle range is another restraint that the fourbar linkage imposes on the mechanism [18]. Although, all these mechanisms limit the flapping angle amplitude except the direct connection of the motor to the wings, but achieving the desired angle amplitude in the four-bar linkage requires some parts with smaller dimensions that is challenging to the manufacturing of those parts.

After comparing the different mechanisms, we choose the crank-slider mechanism (Fig. 3-a) to use for this apparatus. This mechanism requires a narrow width and allows the motor to spin continuously in one direction while generating a symmetrical and identical flapping motion on the two wings.

In this section we first present the kinematic analysis of the mechanism. Then, we derive the dynamical model of the moving parts to analyze the response and design the required gear ratio and the motor requirements. Finally, we present the aerodynamic force and torque on the wings as they are needed in the dynamical analysis.

2.1 Kinematics of the Crank-Slider Mechanism

We use the slider-crank mechanism (Fig. 5) to generate a flapping motion on the wings using a single motor rotating continuously in one direction. In addition to the movement of the motor, the dimensions in the mechanism determine the behavior of the flapping motion on the wings. Therefore, one of the objectives is to determine the geometry of the mechanism to result in the desired wing motion with a unidirectional motor speed control (MSC).

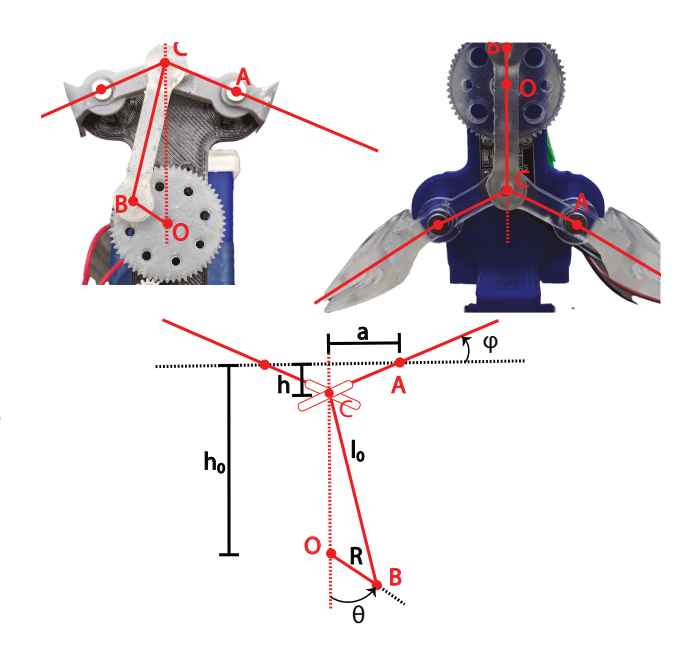


Fig. 5. The mechanism converts the unidirectional motor rotation to the flapping motion on the wings with a single motor. It should be noted that in this mechanism, the length AC varies during a wingbeat cycle and therefore the wing gripper is slotted at point C. The two prototypes (top) and the general configuration of the mechanism (bottom) are shown. The movement of the pin C is assumed positive downward and the angles θ and φ are positive counterclockwise.

To find the geometric relationship between the wing kinematics, flapping angle (ϕ) and flapping angular velocity $(\dot{\phi})$, and the motor motion $(\theta_m, \dot{\theta}_m)$, we start from the flapping angle (ϕ) and move sequentially toward the motor. First, in Fig. 5 we can find the relationship between the vertical movement of the pin C (h) and the wing angle (ϕ) as: $\tan(\phi) = \frac{h}{a}$. Differentiating this equation gives us the vertical velocity of point C as a function of the flapping kinematics $(\phi$ and $\dot{\phi})$: $\dot{h} = a\dot{\phi}(1 + \tan^2(\phi))$

Then, in order to find the relationship between the flapping angle (ϕ) and the crank angle (θ), we use the cosine law in $\triangle OBC$ (Fig. 5):

$$l_0^2 = (h_0 - h)^2 + R^2 + 2R(h_0 - h)\cos(\theta)$$
 (1)

The amplitude of the positive (downward) and negative (upward) vertical movement on pin C can be obtained by setting $\theta=0$ and $\theta=\pi$ respectively in equation 1. Then, by equating the amplitude of the upward and downward movements of pin C we can find the condition for an equal upstroke and down-stroke flapping angle amplitude which re-

sults in $h_0 = l_0$. By substituting this condition in equation 1 and solving for h, we can obtain:

$$h = l_0 + R\cos(\theta) - \sqrt{l_0^2 - R^2\sin^2(\theta)}$$
 (2)

The flapping angle ϕ can be related to θ by substituting $h = a \tan(\phi)$ in equation 2 and the flapping angular velocity $(\dot{\phi})$ can be found by differentiating the resulting equation with respect to time as follows:

$$\tan(\phi) = \frac{l_0}{a} + \frac{R}{a}\cos(\theta) - \sqrt{(l_0/a)^2 - (R/a)^2\sin^2(\theta)}$$

$$\dot{\phi} = \frac{\dot{\theta}}{(1 + \tan^2(\phi))} \left(-\frac{R}{a}\sin(\theta) + \frac{(R/a)^2\sin(\theta)\cos(\theta)}{\sqrt{(l_0/a)^2 - (R/a)^2\sin^2(\theta)}} \right)$$
(4)

By using these equations, we can construct the phase portraits of the wing kinematics $(\dot{\phi} - \phi)$ over one complete wingbeat cycle. Figure 6 shows the wing phase portraits for different dimensionless l_0/a and R/a values based on the above kinematic equations. Each of the 9 graphs in Fig. 6 presents the flapping angular velocity $(\dot{\phi})$ with the unit of [Rad/Sec] as the vertical axis and the flapping angle (ϕ) with the unit of [Rad] as the horizontal axis over a wingbeat cycle resulting from the corresponding l_0/a and R/a values.

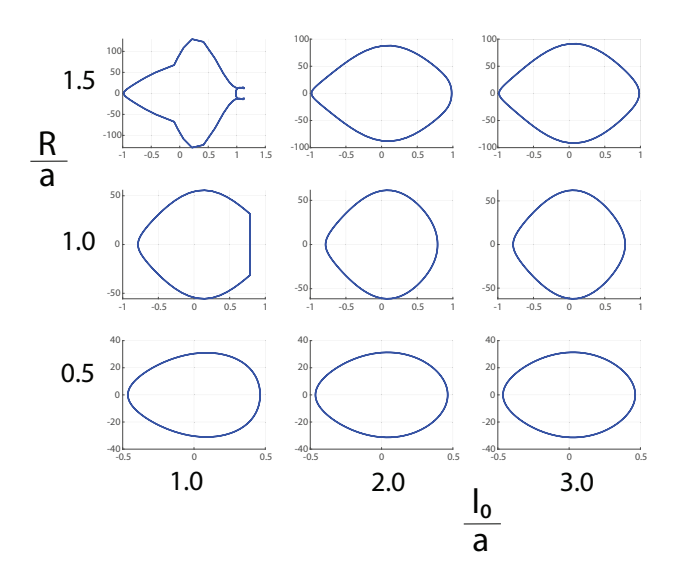


Fig. 6. Wing kinematic phase portraits $(\dot{\phi}[Rad/sec] - \phi[Rad])$ for each individual graph at different dimensionless l_0/a and R/a values for a complete wingbeat cycle.

The results in Fig. 6 shows that for some combinations of l_0/a and R/a, the response is not smooth and sometimes singular. Therefore, we choose the geometric ratios to be

 $\frac{l_0}{a}=2.0$ and $\frac{R}{a}=\frac{1}{\sqrt{3}}\approxeq 0.57$ to first and foremost avoid singularities and abrupt changes. Secondly, due to the flapping angle amplitude to be $\phi_0=30^\circ$ (Fig. 7) to avoid the wing high speeds at the mid upstrokes and down-strokes. Moreover, the capabilities and resolution of the resin printer and the manufacturing tolerance must be taken into account. Therefore, given the wind tunnel dimensions presented in Fig. 2, the geometric dimensions of the mechanism are chosen as: R=1.0 cm, $a=1.75 \approxeq \sqrt{3}$ cm and $l_0=2a=3.5$ cm.

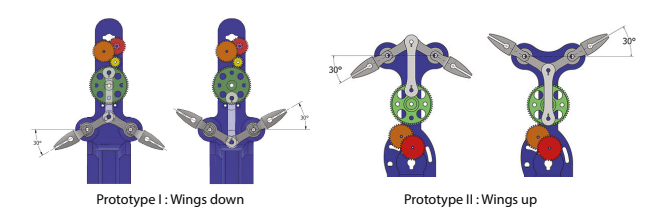


Fig. 7. The CAD model of the two prototypes for the apparatus with the flapping angle amplitude of $\phi_0 = 30^\circ$.

2.2 Dynamics of the Wing

To model the dynamics of the entire wing, we integrate the mechanical equations of motion of the mechanism with the electrical and mechanical dynamics of the motor and include the aerodynamic forces on the wing. We here start by the mechanical dynamics of the motor:

$$J_m \ddot{\Theta}_m + B_m \dot{\Theta}_m = \tau_m - \tau_{ext} \tag{5}$$

Where θ_m is the motor angle, J_m and B_m are the rotational inertia and damping respectively. The motor torque is represented by τ_m , and τ_{ext} is the external torque that the motor can apply to actuate the mechanism. The electrical equation of the motor that relates the current, voltage and the motor rotational velocity can be written as:

$$v_m - R_m i_m = k_m \dot{\Theta}_m \tag{6}$$

Where v_m and i_m are the voltage and the current sent to the motor respectively. The motor winding resistance is represented by R_m which we assume to be constant through the operation and k_m is the motor torque constant. Moreover, the motor torque, current, and the torque constant are related via $\tau_m = k_m i_m$. By substituting these equations into the motor dynamics (equation 5) and considering the effect of the gear ratio N_g that maps the motor angle to the crank angle ($\theta_m = N_g \theta$), we obtain:

$$J_m N_g \ddot{\theta} + (B_m + \frac{k_m^2}{R_m}) N_g \dot{\theta} = \frac{k_m}{R_m} v_m - \tau_{ext}$$
 (7)

Now, we construct the dynamics of the wing by using the Lagrangian approach given the θ (crank angle in Fig. 5) as the single degree of freedom:

$$\frac{d}{dt}\frac{\partial L}{\partial \dot{\theta}} - \frac{\partial L}{\partial \theta} = N_g \tau_{ext} + 2Q_{aero}$$
 (8)

Where L is the Lagrangian of the system, N_g is the gear ratio and τ_{ext} is the torque that the motor can apply to the mechanism. Also, Q_{aero} represents the generalized torque due to the aerodynamic resistance by each wing (the number 2 is for two wings) and can be calculated by equating the virtual work principle using the following equation:

$$Q_{aero} = \tau_{aero} \frac{\partial \phi}{\partial \theta}$$

Here, τ_{aero} is the aerodynamic torque on each wing (section 2.3) and equation 3 is used for finding $\frac{\partial \phi}{\partial \theta}$. After these substitutions, the equations of motion for the wing can be written as:

$$\mathcal{D}(\theta)\ddot{\theta} + \mathcal{C}(\theta,\dot{\theta})\dot{\theta} + \mathcal{G}(\theta) = N_g \tau_{ext} + 2Q_{aero}$$
 (9)

Since the dynamics equation here represents a single degree of freedom system, \mathcal{D} and \mathcal{C} are scalars representing the equivalent mass and centrifugal effect (instead of matrices). \mathcal{G} is the effect of the gravitational force which we ignore due to its small effect in this project as the majority of the inertia is in rotational motion rather than vertical movement. After substituting τ_{ext} in equation 5 into equation 9, we can find the final equation of motion of the system relating the input voltage to the movement of the crank angle (θ) :

$$(\mathcal{D}(\theta) + N_g^2 J_m) \frac{\mathrm{d}^2 \theta}{\mathrm{d}t^2} + (\mathcal{C}(\theta, \dot{\theta}) + N_g^2 (B_m + \frac{k_m^2}{R_m})) \frac{\mathrm{d}\theta}{\mathrm{d}t}$$

$$= \frac{N_g k_m}{R_m} v_m + 2 Q_{aero} \quad (10)$$

In this equation v_m is the input voltage to the motor and θ is the output which, by using equation 3, can be related to the wing kinematics (ϕ and $\dot{\phi}$).

For the simulation we use MATLAB (R2022b, Mathworks Inc., Natick, MA, USA) and its built-in integrator *ode45* that uses Runge-Kutta 4th and 5th order formulas for solving the differential equations. The convergence is determined by checking the error from the relative and absolute tolerances that we choose to be 1×10^{-9} .

To find a proper gear ratio for this apparatus, we simulate the dynamics of the system (equation 10) for different gear ratios. Figure 8 shows how the flapping frequency is

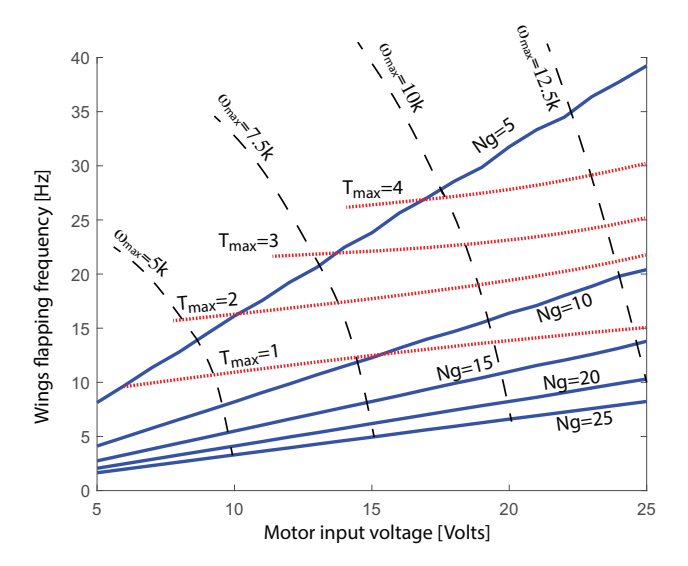


Fig. 8. The effect of the gear ratio on the flapping frequency of the wings. There are two contour lines overlapped, one is the maximum required motor torque $T_{max}[mN.m]$ and the other is the maximum motor angular velocity $\omega_{max}[\text{rev./min.}]$.

affected by the gear ratio and the required motor maximum torque and rotational velocity. Using the results in Fig. 8 and after considering the spur gear dimensions and arrangements through CAD modeling trials, we choose a gear ratio of $N_g=18$ to achieve a flapping frequency of at least 10 hertz at 24 volts. Figure 9 shows the wing flapping angle and angular velocity from the simulation. More details about the gear selection will be discussed later in the paper.

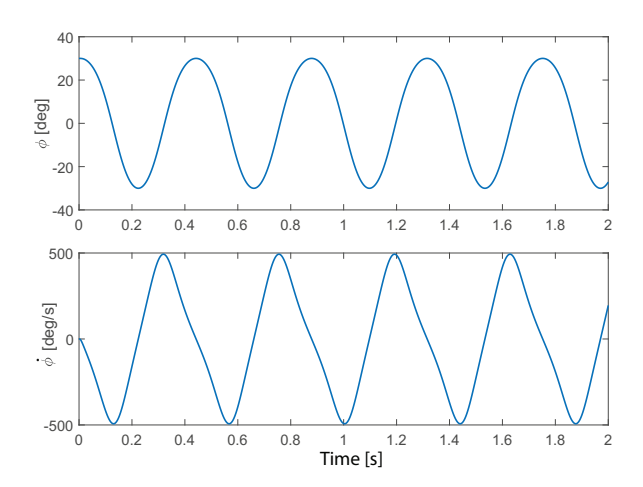


Fig. 9. The flapping angle (ϕ) and wing angular velocity $(\dot{\phi})$ responses under a constant input voltage.

2.3 Aerodynamics

To model the effect of the aerodynamic forces on the flapping wings we use the quasi-steady formulation [16–19]. Since the goal is to install the apparatus in the wind tunnel,

the effective wind velocity on each element along the wings has free-stream (V_{∞}) and flapping $(r\dot{\phi})$ components (Fig. 10). Then, the aerodynamic force on each element along the wing can be decomposed into a normal (dN) and tangential (dT) components [20] with respect to the wing surface.

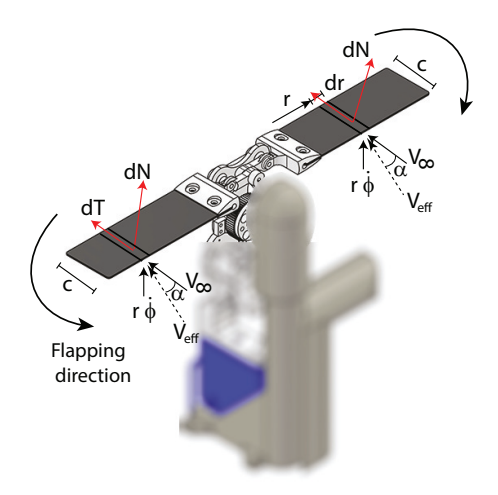


Fig. 10. The normal (dN) and tangential (dT) aerodynamic forces are applied on each element based on the effective velocity ($V_{\rm eff}$) and angle of attack (α) that changes along the wing due to the change in the distance from the wing root (r).

The incremental aerodynamic torque due to each element $(d\tau_{aero})$ is:

$$d\tau_{aero} = rdN = \frac{1}{2}\rho C_N(\alpha)(V_{\infty}^2 + (r\dot{\phi})^2)crdr$$

The normal force coefficient can be assumed as $C_N(\alpha) = a_N \sin(\alpha)$ [17,20]. Where $a_N = 3.4$ and α is the effective angle of attack which varies along the wing due to the flapping velocity component $(r\dot{\phi})$. Due to the zero pitch orientation of the apparatus $\tan(\alpha) = \frac{r\dot{\phi}}{V_{\infty}}$ and therefore, the incremental aerodynamic torque can be written as:

$$d\tau_{aero} = \frac{1}{2} \rho a_N \sin(\alpha) (V_{\infty}^2 + (r\dot{\phi})^2) crdr$$

Since for the possible effective angle of attack range of $-\frac{\pi}{2} \leq \alpha \leq \frac{\pi}{2}$ one can use $\sin(\alpha) = \frac{\tan(\alpha)}{\sqrt{1+\tan^2(\alpha)}}$ and considering $\tan(\alpha) = \frac{r\dot{\phi}}{V_{\infty}}$ then:

$$\mathrm{d}\tau_{aero} = \frac{1}{2}\rho a_N(r\dot{\phi})\sqrt{(V_\infty^2 + (r\dot{\phi})^2)}cr\mathrm{d}r$$

By integrating this equation along the wing length we can find the aerodynamic torque as:

$$\begin{split} \tau_{aero} &= \int_0^{R_w} \frac{1}{2} \rho a_N(r\dot{\phi}) \sqrt{(V_\infty^2 + (r\dot{\phi})^2)} c r \mathrm{d}r \\ &= \frac{1}{2} \rho c a_N \dot{\phi} \int_0^{R_w} r^2 \sqrt{(V_\infty^2 + (r\dot{\phi})^2)} \mathrm{d}r \\ &= \frac{1}{2} \rho c a_N \frac{V_\infty^4}{\dot{\phi}^2} f(\eta) \end{split}$$

Where
$$f(\eta) = \sqrt{1 + \eta^2} (\frac{\eta^3}{4} + \frac{\eta}{8}) - \frac{1}{8} \ln(\eta + \sqrt{1 + \eta^2})$$
 and $\eta = \frac{R_w \dot{\phi}}{V_{co}}$.

The aerodynamic torque generated on each wing is shown in Fig. 11 for different free-stream velocities at a constant flapping frequency.

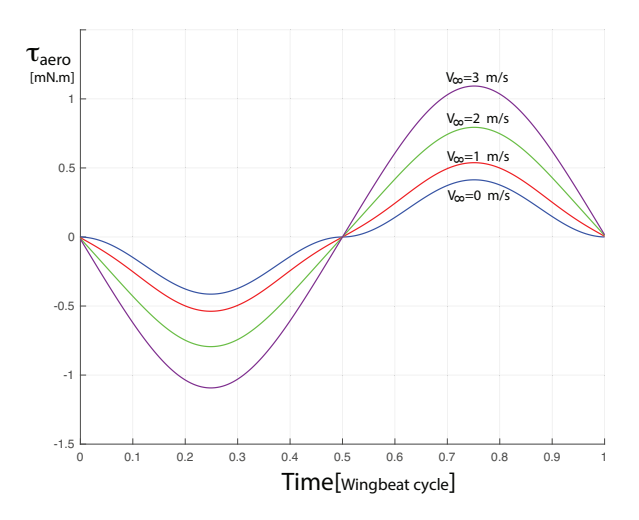


Fig. 11. The aerodynamic torque generated on each wing at different free-stream velocities and given a wingbeat frequency of 5 Hz. for one wingbeat cycle.

3 Integration and Manufacturing

In this section we explain how the different components were designed in CAD, manufactured, and integrated into two prototypes shown earlier. We start with the wings, then we present the design process for the chassis prototypes followed by the gear arrangements in the transmission.

3.1 Wing Element and Attachment

The wings' dimension are determined based on the geometry of the wind tunnel, the chassis, and the mechanical characteristics of the materials. The wings' length are directly determined based on the cross section size of the wind tunnel presented earlier (Fig. 2). To avoid the boundary effect from the wind tunnel walls we choose the wings' length to be 10 cm across all the samples. Moreover, the wings should sustain the stress due to aerodynamic forces and stay

in the elastic region because of the repeatability of the flapping motion. To accomplish this goal, we use the maximum aerodynamic torque on the wings to confirm the integrity of the material and the wing thickness to stay in the elastic region.

The wing samples are 100mm x 40mm length by width sheets and thicknesses ranging from 0.09mm to 1.70mm (Fig. 12). The materials are a spread of varying metals, plastics, and composites forming a total of 24 wing trials.

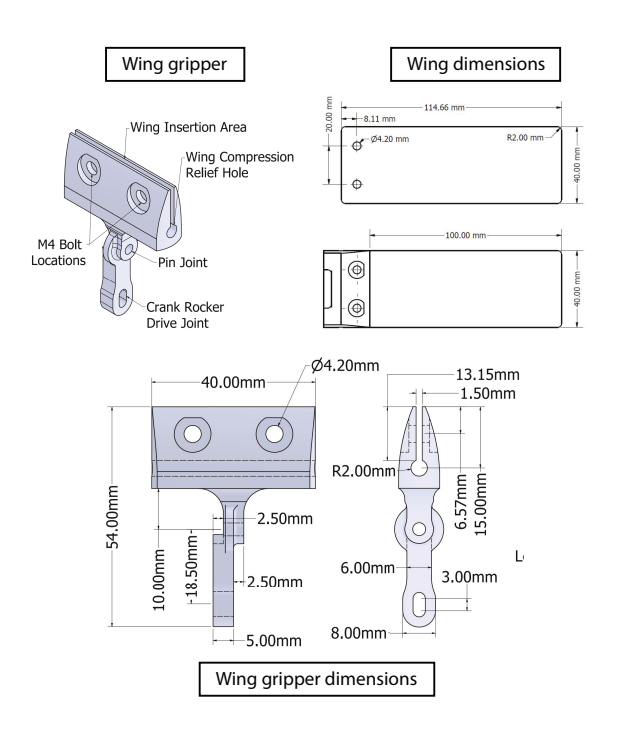


Fig. 12. Wing and the wing holder dimensions

To connect the wings to the crank-slider mechanism, two wing grippers with press fit engagement are used (Fig. 12). They are designed to pivot around a pin at their midpoint where they are installed on the chassis to transform the linear movement of the crank-slider mechanism to flapping motion on the wings. It should be noted that the attachment points on the wing holder needs to be slotted to allow for the desired flapping angle amplitude of $\pm 30^{\circ}$ (Fig. 7).

For assembling reasons, at the wing insertion area's innermost section, a relief hole is needed to assist with linear clamp load on the wing element (Fig. 12). Also, we use two M4 screws retained with machine nuts while isolated from the resin material with 9mm diameter machine washers. We realized through wing actuation trials that nylon M4 hardware is preferable for wing retention due to its weight and adequate grip instead of the alloy steel counterpart. Furthermore, a 2.5mm offset feature on the midsection of the wing gripper design is incorporated for crank rocker meshing as well as to allow for a symmetric design.

Finally, to manufacture the gripper we use resin 3D printer and the material selection was determined experimentally. We started by the rigid 4000 grade resin, with a tensile

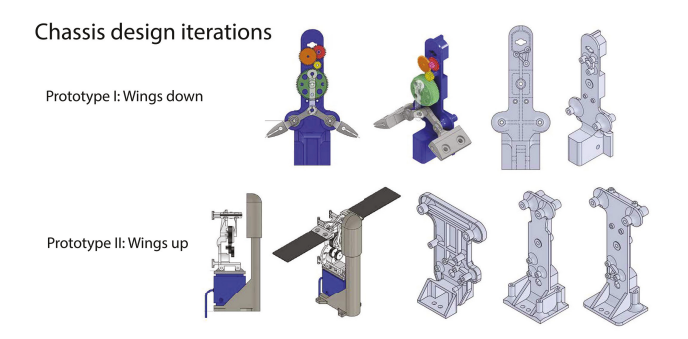


Fig. 13. The Chassis Prototype Iterations

and flexural modulus of 4.1 GPa and 3.4 GPa respectively with a tensile strength of 69 MPa. We found out that the wing holders constructed with the Rigid 4000 grade resin are prone to fractures during assembly and handling, but performed well for flapping cycles after installation. Due to the need to assemble multiple different wing materials, fractures during assembly would be undesirable. We found the tough 1500 grade resin to be an adequate alternative with a tensile and flexural modulus of 1.5 GPa and 1.4 GPa respectively.

3.2 Chassis Design

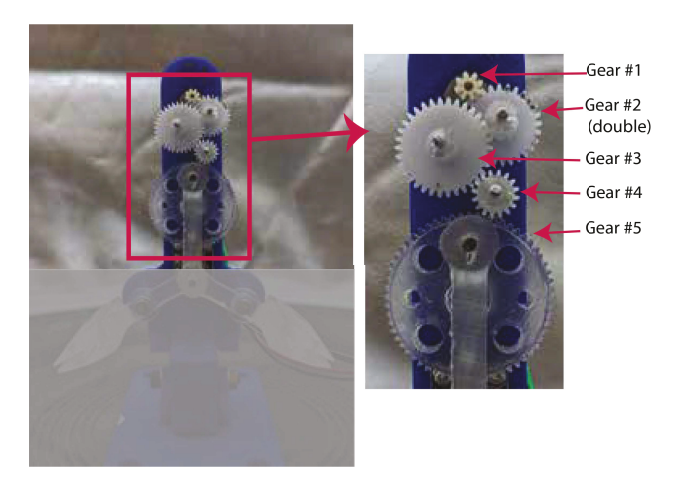
The chassis is the central part of this apparatus on which the different elements including the transmission, the DC motor, and the wings are installed. Moreover, the chassis should be designed to comply with the installations and provide a reasonable tolerance for installing purposes. We developed the chassis in iterations through multiple 3D printing trials given the design constraints we explained in section 2. Figure 13 shows the chassis iterations for the two prototypes we developed for this apparatus. It should be noted that the chassis needs to rigidly retain the DC motor, gear assembly, and the wing actuation linkages. Moreover, it should provide a fixed mounting location for the force sensor at the bottom as well as the ability to be mounted in the wind tunnel. The wind tunnel access point shown in Fig. 2 sets a target height for the entire apparatus and subsequently for the chassis.

The chassis is designed to incorporate the DC motor into the rear of the gearbox and to drive the transmissions via the motor integrated spur gear. We found out that gear interference is sensitive to 3D printer model and filament size which warranted dedicating a single 3D printing setup for chassis construction. We experimented several combinations of gear arrangements to find an appropriate design with a minimum number of moving components to be installed on the chassis. Then, the locations of the gears are designed in the CAD model of the chassis for 3D printing to ensure size and fitting compatibility.

3.3 Transmission Design

The transmission is powered by a DC motor and a series of single and double spur gears. To achieve a gear ratio of $N_g = 18$ as explained in section 2, we combined multiple spur gears in CAD to fit the geometry and reach the desired

gear ratio (Fig. 3.3). The DC motor utilizes an integrated 8 tooth spur gear and is press fit into the 3D printed chassis. We installed the other die cast plastic gears on the chassis using the 2mm steel rod and pressed fit them into the proper locations on the chassis.



Gear Assembly		
Gear Type	Tooth Count	Thickness (mm)
Spur (Gear #1)	8	4
Double Spur	24, 10	1.5, 3.5
(Gear #2)		
Spur (Gear #3)	34	1.5
Spur (Gear #4)	16	5.0
Crank Spur	60	7.0
(Gear #5)		

Fig. 14. Assembled Gearbox

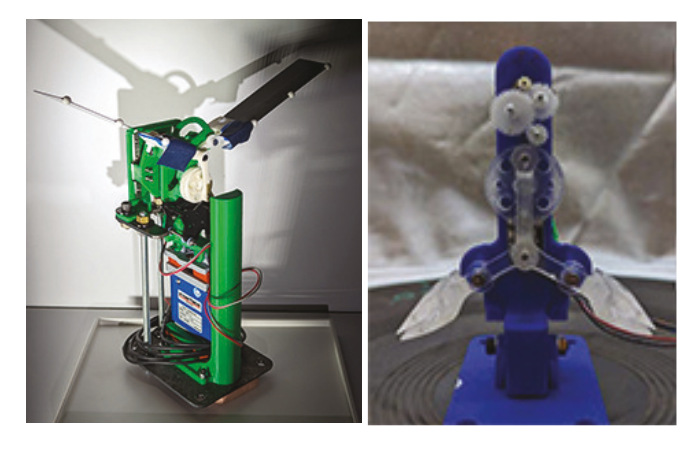


Fig. 15. The constructed prototypes of the flapping wing apparatus.

4 Experiment Verification

Figure 16 shows the setup of our experiment to verify the proper movement of the wings. We used marker tracker

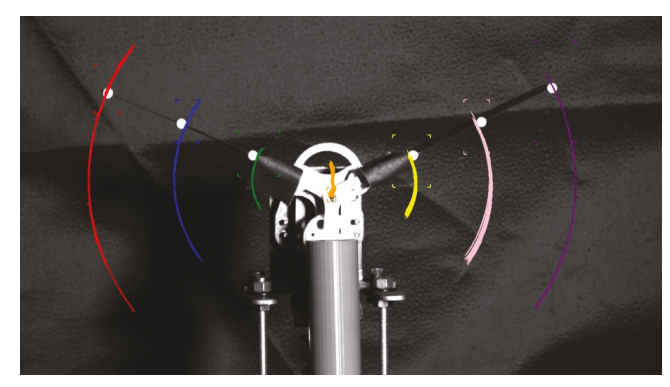


Fig. 16. A screenshot of the experiment setup to measure the wing kinematics at a given constant voltage.

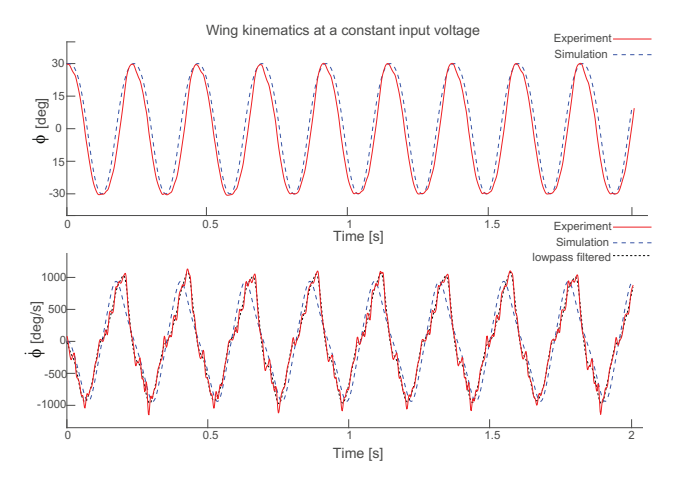


Fig. 17. The flapping angle (ϕ) and the flapping angular velocity $(\dot{\phi})$ from experiment and simulation.

in order to track the movements of different points along the wings and the mechanism. Figure 17 shows the flapping angle and its velocity in simulation and experiment at a given constant voltage to the motor. Since the flapping angular velocity signal $(\dot{\phi})$ is noisy, we present a low-pass filter signal as well. The results show that the wing kinematics from the experiment $(\phi$ and $\dot{\phi})$ match the simulation and confirms the design of the mechanism.

5 Conclusion

In this paper we presented our process for the design and manufacturing of a flapping wing apparatus to be installed in a wind tunnel. First, we compared different alternatives for the flapping wing mechanism and selected the crank-slider mechanism given the requirements for our apparatus. Then, we presented the design process for this mechanism using both kinematic analysis and the dynamics of the entire system including the dynamics of the motor (both mechanical and electrical equations of the electric motor). We used the dynamics equation that relates the input voltage to the flapping motion on the wings in order to include the effect of the dynamical characteristics like motor inertia and damping on the performance of the apparatus in the design pro-

cess. Using the dynamics of the entire system, we presented the design process to select the proper electric motor for the mechanism. Moreover, we presented the trade-off between the gear ratio, motor maximum angular velocity and motor maximum torque. For the aerodynamic torque, we used a quasi-steady formulation and developed a closed form formulation for such a flapping wing system in the presence of free-stream wind velocity for the purpose of design. This formulation can be used for selecting the motor and designing the wing structure in flapping wing robots for hovering and/or forward flight. We presented the process for manufacturing the parts of the apparatus and how we made the decisions for material selection and manufacturing method selection including 3D printing, resin printing, etc. for different parts of the apparatus. In presenting the manufacturing process we articulated the design constraints and the effect of the manufacturing limitations on the behavior of the mechanism. Furthermore, we discussed how the manufacturing limitations affected the design decisions during mechanism selection and design. Finally, we presented the constructed prototypes and the results from the experiment to confirm the design and manufacturing process.

Acknowledgment

This work is supported by the National Science Foundation grant 1931122.

References

- [1] Ramezani, A., Chung, S.-J., and Hutchinson, S. (2017), A biomimetic robotic platform to study flight specializations of bats, *Science Robotics* **2**, eaal2505.
- [2] Tu, Z., Fei, F., Zhang, J., and Deng, X. (2020), An atscale tailless flapping-wing hummingbird robot. i. design, optimization, and experimental validation, *IEEE Transactions on Robotics* **36**, 1511–1525.
- [3] Wood, R. J. (2008), The first takeoff of a biologically inspired at-scale robotic insect, *IEEE Transactions on Robotics* **24**, 341-347.
- [4] He, G., Su, T., Jia, T., Zhao, L., and Zhao, Q. (2020), Dynamics Analysis and Control of a Bird Scale Underactuated Flapping-Wing Vehicle, *IEEE Transactions* on Control Systems Technology 28, 1233–1242.
- [5] Deng, H., Xiao, S., Huang, B., Yang, L., Xiang, X., and Ding, X. (2020), Design optimization and experimental study of a novel mechanism for a hover-able bionic flapping-wing micro air vehicle, *Bioinspiration & Biomimetics* **16**, 026005.
- [6] Phan, H. V., Aurecianus, S., Kang, T., and Park, H. C. (2019), Kubeetle-s: An insect-like, tailless, hovercapable robot that can fly with a low-torque control mechanism, *International Journal of Micro Air Vehi*cles 11, 1756829319861371.
- [7] Marshall, K. L., Chadha, M., deSouza, L. A., Sterbing-D'Angelo, S. J., Moss, C. F., and Lumpkin, E. A. (2015), Somatosensory substrates of flight control in bats, *Cell Reports* 11, 851-858.

- [8] Rummel, A. D., Sierra, M. M., Quinn, B. L., and Swartz, S. M. (2023), Hair, there and everywhere: A comparison of bat wing sensory hair distribution, *The Anatomical Record* 306, 2681–2692.
- [9] Fabian, J., Siwanowicz, I., Uhrhan, M., Maeda, M., Bomphrey, R. J., and Lin, H.-T. (2022), Systematic characterization of wing mechanosensors that monitor airflow and wing deformations, *Iscience* 25.
- [10] Roshanbin, A., Altartouri, H., Karásek, M., and Preumont, A. (2017), Colibri: A hovering flapping twin-wing robot, *International Journal of Micro Air* Vehicles 9, 270–282.
- [11] McGill, R., Hyun, N.-s. P., and Wood, R. J. (2022), Frequency-modulated control for insect-scale flapping-wing vehicles, *IEEE Robotics and Automation Letters* 7, 12515–12522.
- [12] Tijmons, S., Karásek, M., and De Croon, G. (2018), Attitude control system for a lightweight flapping wing may, *Bioinspiration & biomimetics* **13**, 056004.
- [13] Chirarattananon, P., Chen, Y., Helbling, E. F., Ma, K. Y., Cheng, R., and Wood, R. J. (2017), Dynamics and flight control of a flapping-wing robotic insect in the presence of wind gusts, *Interface focus* 7, 20160080.
- [14] Pellerito, V. and Vejdani, H. (2019), The effect of wing-motor connection mechanism on the payload capacity of flapping flight hovering robots, in *Dynamic Systems and Control Conference*. volume 59155. p. V002T25A006. American Society of Mechanical Engineers.
- [15] Vejdani, H., Haji, L., Fernandez, V., and Jawad, B. (2022), Mechanism design and control of a winged hovering robot with flapping angle constraint, ASME Letters in Dynamic Systems and Control 2, 041002.
- [16] Vejdani, H. R., Boerma, D. B., Swartz, S. M., and Breuer, K. S. (2018), The dynamics of hovering flight in hummingbirds, insects and bats with implications for aerial robotics, *Bioinspiration & Biomimetics* 14, 016003
- [17] Mahjoubi, H. and Byl, K. (2012), Steering and horizontal motion control in insect-inspired flapping-wing mays: The tunable impedance approach, in 2012 American Control Conference (ACC). pp. 901–908.
- [18] Vejdani, H., Fan, X., and Breuer, K. (2022), Robustness analysis of minimally-actuated flapping wing systems due to aerodynamic modeling uncertainty, in 2022 IEEE/ASME International Conference on Advanced Intelligent Mechatronics (AIM). pp. 670–676. IEEE.
- [19] Vejdani, H., Boerma, D., Swartz, S. M., and Breuer, K. S. (2017), Guidelines for the design and control of bio-inspired hovering robots, in 2017 IEEE International Conference on Robotics and Automation (ICRA). pp. 4160–4166. IEEE.
- [20] Byl, K. (2010), A passive dynamic approach for flapping-wing micro-aerial vehicle control, ASME 2010 Dynamic Systems and Control Conference, Volume 1. pp. 215–223.